Jpn. J. Appl. Phys. Vol. 38 (1999) pp. 6890–6895
Part 1, No. 12A, December 1999

Two-Dimensional Fluid Simulation and Langmuir Probe Measurement of a Planar Inductively Coupled Oxygen Plasma

Hyun Jin YOON, Tae Hun CHUNG and Dong Cheol SEO
Department of Physics, Dong-A University, Pusan 604-714, Korea

(Received July 21, 1999; revised manuscript received September 20, 1999; accepted for publication September 21, 1999)

A two-dimensional (2D) self-consistent axisymmetric fluid simulation of an inductively coupled discharge of electronegative oxygen plasma with a one-turn antenna placed on the top of the dielectric roof is presented. The model equations include continuity equations, the Poisson equation, and an electron energy balance equation. For a planar inductive discharge, the electric field component $E_\theta(r, z)$ is calculated, assuming axisymmetric geometry. Considering a deep penetration of the induced rf field, the power deposition profile is formulated and used as the electron heating term in the electron energy balance equation. The 2D distributions of charged particle densities, electric potential, electron temperature, and ionization rate are calculated and compared with experiments. The effect of neutral gas pressure on plasma characteristics is investigated. As a result, for a relatively low pressure (5 mTorr) case, the ionization rate and charged particle densities are uniform in the radial direction, and for a medium pressure (20 mTorr) case, the ionization rate and the negative ion density are sharply maximized in the axial and radial directions. The results of the simulation agree reasonably well with the results of the spatially averaged global model and experimental results.

KEYWORDS: planar inductively coupled plasma source, rf oxygen discharge, two-dimensional fluid simulation

1. Introduction

For a large area wafer processing and submicron dry etching, a low pressure and a high density plasma with very good radial uniformity are required. One of the most promising plasma sources toward this trend is the inductively coupled plasma (ICP) source. The planar ICP discharge source consists of a spiral, inductive coil on an upper quartz window. RF power continuously applied to the coil induces azimuthal electric fields that partially ionize gas inside the chamber and sustain a discharge. To control the ion energies incident on the wafer, the substrate can be optionally biased by independently applying a rf potential. To investigate plasma generation mechanisms and plasma transport in ICP reactors, simulation models have been developed.[1–6)]

Oxygen discharges are widely used to sputter-deposit aluminum or tungsten, grow SiO_2 film on silicon, and remove photoresist or polymer film. Numerical modeling of oxygen glow discharge can provide insight on the physical phenomena in the discharge and lead to a better understanding and design of the reactor used for the purpose of the thin-film deposition. Due to the increased interest in various high-density plasma sources along with large area wafer processing and stringent uniformity requirements, the demand for the development of two-dimensional (2D) models is ever increasing. Although a typical ICP reactor has a low aspect ratio geometry which resembles that of rf diodes, 2D models are necessary, since the power coupling is spatially nonuniform.

2D fluid models of charged particle distribution appear to be useful in the effort to understand the physical structure of the discharge. Boeuf[7,8)] and Pitchford[9)] studied both a helium discharge and a model electronegative discharge. They used the local field equilibrium approximation (LFA), omitting the electron energy equation. The charged particle fluxes consist of a term representing drift due to the electric field and a diffusion term. This model includes a continuity equation for electrons and ions and Poisson's equation for the electric field. Fluid simulations including an energy balance equation have been performed in one-dimensional (1D) space[10–14)] and in 2D space.[15,16)]

In this paper, we present a numerical description of rf discharge based on a 2D fluid model including an electron energy equation in which various electron energy loss mechanisms can be considered. Outputs such as the spatial distributions of the ionization rate, charged particle density, potential (electric field), and electron temperature are displayed on a video monitor with 2D or 3D interactive graphics using Xgrafix.[17)] A 2D simulation can also account for the uniformity of the ion fluxes toward the substrate. The simulation results we report in this paper were intended to model the discharge experiment being performed, and we compare it with the experimental measurement. In addition, we intend to discuss some general features of ICP discharges, and to analyze the influence of neutral gas pressure on the characteristics of the oxygen discharge. The effect of the pressure on the radial uniformity is studied over the range of 1–20 mTorr for nonuniform power deposition profile calculated by an electromagnetic module. This paper is organized as follows: in §2 a physical model and basic equations are presented, in §3 experimental equipment and Langmuir probe diagnostics are described, in §4 simulation results are presented and discussed, and comparison with experiments is made, and in §5 conclusions are summarized.

2. Physical Model and Basic Equations

A schematic of an ICP reactor is shown in Fig. 1. The plasma chamber is a stainless-steel cylinder with inside diameter of 30 cm and height of 50 cm. This configuration is chosen to accommodate wafers of the desired size, and to position the substrate holder over the long range. The plasma is generated by an inductively coupled azimuthal electric field with a one-turn antenna. Our model for ICP reactors is a hybrid simulation consisting of an electromagnetic module and a 2D fluid simulation to obtain species densities and fluxes as a function of position (r, z). The simulation begins by calculating the coil-generated electric and magnetic fields, $B_r(r, z)$, $B_z(r, z)$, and $E_\theta(r, z)$. We estimate the field components induced by the antenna. To simplify the problem, we make two approximations. First, we introduce a vacuum field model where we assume the coil to be in free space with no bound-

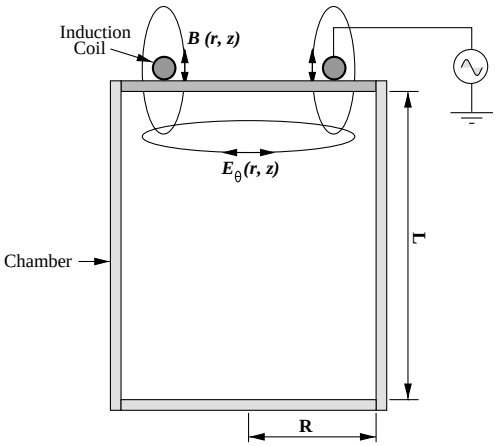

Fig. 1. Schematic of the inductively coupled plasma reactor. The circular cross-section coil is driven at 13.56 MHz and placed on a dielectric roof. The spiral coil produces magnetic field $B_z(r, z)$ which generates an azimuthal electric field $E_\theta(r, z)$.

aries. In other words, we neglect the effect of the chamber walls on the magnetic induction. The validity of this approximation has been addressed previously.[18] Second, we assume the helical planar coil to consist of a one-turn concentric loop of radius a. In our case, $a = 10$ cm. The nonzero vector potential and the magnetic induction components for the loop are given by Symthe[19] for a loop with center located at $r = 0$ cm, $z = 0$ cm. The vector potential for the one-turn coil, $A_\theta(r, z)$, is given as[19]

$$A_\theta(r, z) = \frac{\mu_0}{\pi}\frac{I_{\rm rf}}{\kappa}\left(\frac{a}{r}\right)^{\frac{1}{2}}\left[\left(1-\frac{1}{2}\kappa^2\right)K(\kappa)-E(\kappa)\right]. \tag{2.1}$$

Here, μ_0 is the permeability of free space and $I_{\rm rf}$ is the applied rf current to the antenna coil.

The magnetic field induction for the one-turn loop along the axis of the system is

$$B_z(r, z) = \frac{\mu_0 I_{\rm rf}}{2\pi}\frac{1}{\left((a+r)^2+z^2\right)^{\frac{1}{2}}} \times\left[K(\kappa)+\frac{a^2-r^2-z^2}{(a-r)^2+z^2}E(\kappa)\right], \tag{2.2}$$

where $K(\kappa)$ and $E(\kappa)$ are the complete elliptic integrals of the first and second kinds respectively, and r is the radial position as measured from the axis of the system. The parameter κ is defined by

$$\kappa^2 \equiv \frac{4ar}{z^2+(a+r)^2}. \tag{2.3}$$

The electric field is $E_\theta(r, z) = -j\omega A_\theta$, and $\boldsymbol{E}$ and $\boldsymbol{B}$ are related by Faraday's law. Assuming cylindrical symmetry, we have

$$E_\theta(r, z) = -\frac{1}{r}\int_0^L r'\dot{B}_z(r', z)dr', \tag{2.4}$$

where r and r' are the radial positions as measured from the axis of the system and in the sinusoidal steady state, $\dot{B}_z(r, z) = \omega B_z(r, z)$. The power dissipated within the plasma is given by

$$P_{\rm abs}(r, z) = {\rm Re}\left(\sigma_{\rm p}|E_\theta(r, z)|^2\right), \tag{2.5}$$

where $\sigma_{\rm p}$ is the plasma conductivity

$$\sigma_{\rm p} = \frac{e^2 n_{\rm e}}{m(\nu_{\rm eff}+j\omega)}, \tag{2.6}$$

$\nu_{\rm eff}$ $(= \nu_{\rm en} + \nu_{\rm stoc} + \nu_{\rm ei})$ is the effective collision frequency which includes electron-neutral collision, stochastic collision and electron-ion collision, $n_{\rm e}$ is the electron density and ω is the frequency of the driving rf.

The basic assumptions of the model are as follows: (1) the particle motion is collision dominated, and as a result, a fluid model is applicable, (2) the transport parameters, such as mobility and diffusion coefficients of charged particles, are constant, (3) the reaction (ionization, excitation, and recombination) rate for discharge is a function of the electron temperature, (4) the density and the temperature of neutral gas are constant in the chamber, and (5) the gas temperature is 300 K.

At low pressure, the dissociation degree in the discharge is low and the plasma composition can be expected to be simple, with O_2 the dominant neutral species, O^- the dominant negative ion, and O_2^+ the dominant positive ion.[20] The continuum model consists of five equations: electron, positive ion, and negative ion continuity, Poisson's equation, and the electron energy balance equation. Under these assumptions, the model continuity equations are expressed as[12,13]

$$\frac{\partial n_{\rm e}}{\partial t}+\nabla\cdot\boldsymbol{\phi}_{\rm e} = R_{\rm i}-R_{\rm a}, \tag{2.7}$$

$$\frac{\partial n_{\rm p}}{\partial t}+\nabla\cdot\boldsymbol{\phi}_{\rm p} = R_{\rm i}-R_{\rm v}, \tag{2.8}$$

$$\frac{\partial n_{\rm n}}{\partial t}+\nabla\cdot\boldsymbol{\phi}_{\rm n} = R_{\rm a}-R_{\rm v}. \tag{2.9}$$

Instead of solving the momentum balance equation, the drift-diffusion approximation is used for the particle fluxes:

$$\boldsymbol{\phi}_{\rm e} = -D_{\rm e}\nabla n_{\rm e}-n_{\rm e}\mu_{\rm e}\boldsymbol{E}, \tag{2.10}$$

$$\boldsymbol{\phi}_{\rm p} = -D_{\rm p}\nabla n_{\rm p}+n_{\rm p}\mu_{\rm p}\boldsymbol{E}, \tag{2.11}$$

$$\boldsymbol{\phi}_{\rm n} = -D_{\rm n}\nabla n_{\rm n}-n_{\rm n}\mu_{\rm n}\boldsymbol{E}. \tag{2.12}$$

Here, $n_{\rm e(p,n)}$, $D_{\rm e(p,n)}$, and $\mu_{\rm e(p,n)}$ are the density, diffusion coefficient and mobility of electrons, positive ions, and negative ions, respectively. The ionization, dissociative attachment, recombination, and excitation rate terms, $R_{\rm i}$, $R_{\rm a}$, $R_{\rm v}$, and R_{ex}, respectively, are written in the forms

$$R_{\rm i} = k_{\rm i}n_{\rm e}N, \tag{2.13}$$

$$R_{\rm a} = k_{\rm a}n_{\rm e}N, \tag{2.14}$$

$$R_{\rm v} = k_{\rm v}n_{\rm p}n_{\rm n}, \tag{2.15}$$

$$R_{\rm ex} = k_{\rm ex}n_{\rm e}N, \tag{2.16}$$

where N is the density of neutral gas, and the reaction rate coefficients, $k_{\rm i}$, $k_{\rm a}$, $k_{\rm v}$, and $k_{\rm ex}$ are described by mathematical fits to the Boltzmann-solution results. They are written as a function of the electron temperature in Arrhenius form[21]

$$k = AT_{\rm e}{}^B\exp\left(-\frac{C}{T_{\rm e}}\right). \tag{2.17}$$

The model energy balance equation is written as

$$\frac{\partial\left(\frac{3}{2}n_{\mathrm{e}}kT_{\mathrm{e}}\right)}{\partial t}+\nabla\cdot\boldsymbol{Q}_{\mathrm{e}}=-e\boldsymbol{\phi}_{\mathrm{e}}\cdot\boldsymbol{E}-\sum_{l}H_{l}R_{l}+P_{\mathrm{abs}}, \tag{2.18}$$

where k, T_{e}, e, and H_l (l = ionization, excitation) are the Boltzmann constant, electron temperature, electron charge, and the electron energy loss per collision, respectively. The values of the parameters used for the electronegative oxygen discharge are shown in Table I. The heat flux vector is

$$\boldsymbol{Q}_{\mathrm{e}}=-\frac{5}{2}D_{\mathrm{e}}n_{\mathrm{e}}\nabla(kT_{\mathrm{e}})+\frac{5}{2}\boldsymbol{\phi}_{\mathrm{e}}kT_{\mathrm{e}}\,. \tag{2.19}$$

Poisson's equation is expressed as

$$\nabla^2V=-\frac{|e|}{\varepsilon_0}(n_{\mathrm{p}}-n_{\mathrm{e}}-n_{\mathrm{n}}), \tag{2.20}$$

where V and ε_0 are the potential and the permittivity of free space, respectively.

Boundary conditions used in solving eqs. (2.7)–(2.9), (2.18), and (2.20) are $V=0$, $n_{\mathrm{i}}=0$ (i = e, p, n), and $\nabla T_{\mathrm{e}}=0$ at grounded metal walls. The charged particle flux and flux of electron energy are obtained using an exponential scheme.[22] The equations are discretized by the finite difference method for the spatial derivatives, while the time derivations are discretized by forward Euler differencing (FCTS). The numerical method is described in ref. 23.

3. Experimental

The chamber is a stainless-steel cylinder with interior dimensions of 50 cm height and 15 cm radius. A single turn coil is placed 0.2 cm distant from a 1.9-cm-thick quartz plate.

The diagnostic port is at the one-quarter point to the quartz plate along the cylinder axis. The plasma chamber is evacuated by a turbomolecular pump which has a pumping speed of 600 l/s backed by a rotary pump giving a base pressure of about 5–8 $\times 10^{-6}$ Torr. The equilibrium gas pressure in the chamber is monitored using a cold cathode gauge. To further control the chamber pressure, the gate valve could be manually adjusted to vary the pumping speed. The oxygen gas pressure was varied in the range of 1–80 mTorr.

The induction coil is made of copper and connected to a L-type capacitive matching network, a directional coupler (Amplifier Research DC2600), and a power amplifier (ENI A-500) driven by a function generator (Thander TG2002). A disk-type Langmuir probe is used in the experiment to measure the positive ion density, electron density, electron temperature, and plasma potential.

Experiments were conducted at several pressures and powers. In order to allow the chamber to reach equilibrium, the plasma was turned on and allowed to run for an hour before any measurements were taken.

Table I. Gas transport and rate parameter values.

Name	Symbol	O_2
Electron Diffusivity	$N D_{\mathrm{e}}$ (cm s)$^{-1}$	4.17×10^{22}
Positive Ion Diffusivity	$N D_{\mathrm{p}}$ (cm s)$^{-1}$	5.15×10^{17}
Negative Ion Diffusivity	$N D_{\mathrm{n}}$ (cm s)$^{-1}$	6.37×10^{17}
Electron Mobility	$N\mu_{\mathrm{e}}$ (V cm s)$^{-1}$	1.39×10^{22}
Positive Ion Mobility	$N\mu_{\mathrm{p}}$ (V cm s)$^{-1}$	2.00×10^{19}
Negative Ion Mobility	$N\mu_{\mathrm{n}}$ (V cm s)$^{-1}$	2.48×10^{19}

The saturated current above the space potential is given by

$$i_s=eS\left[n_{\mathrm{e}}\left(\frac{T_{\mathrm{e}}}{2\pi m}\right)^{1/2}+n_{\mathrm{n}}\left(\frac{T_{\mathrm{n}}}{2\pi M_{\mathrm{n}}}\right)^{1/2}\right], \tag{3.1}$$

where e is the electronic charge, S is the probe area, m and M_{n} are masses of electrons and negative ions, respectively, T_{n} is the temperature of negative ions.

The positive ion saturation current is

$$i_{+}=0.6eSn_{\mathrm{p}}\left(\frac{T_{\mathrm{e}}}{M_{\mathrm{p}}}\right)^{1/2}, \tag{3.2}$$

where M_{p} is the positive ion mass. We have a density balance between negatively and positively charged particles given by $n_{\mathrm{e}}+n_{\mathrm{n}}=n_{\mathrm{p}}$. By measuring electron and positive ion saturation currents and the slope of the probe i–V curve, one can obtain the densities of electrons, negative ions, positive ions, and the electron temperature.[24] The ratio of T_{e} to T_{n} is assumed to be 50. To determine this ratio more accurately, one must use a separate double probe along with the single probe.[25]

4. Results and Discussion

We consider an empty cylinder, without a substrate plate, although our model is presently capable of including arbitrarily shaped structures in a cylindrically symmetric (r, z) geometry. All chamber walls are considered to be conducting and electrically grounded, and the power coupling from induction coils is treated with the power deposition profile based on a calculated electric field.

Figure 2 shows the spatial distributions of the power deposition based on eq. (2.5) for oxygen plasma at 20 mTorr. Here we use $I_{\mathrm{rf}}=40$ A. The behavior of ICP reactors is largely determined by the spatial variation and the penetration of the azimuthal electric field. The maximum azimuthal electric field is 500 V/m immediately below the dielectric roof. The total deposition power into the plasma reactor is about 200 W. The peak power deposition is 2 W/cm^3 at 1.8 cm below the dielectrics. Since the conductivity determines the penetration of the electric field, small variations in the slopes of either the electric field or conductivity result in larger variations in the power deposition.

In Fig. 3, 2D spatial profiles for potential V, ionization rate

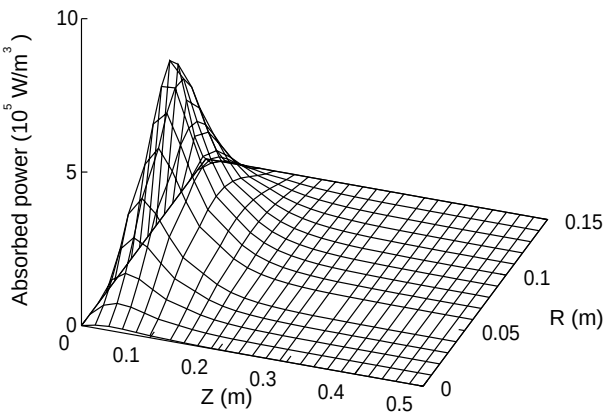

Fig. 2. Profiles of absorbed power for oxygen plasma at 20 mTorr.

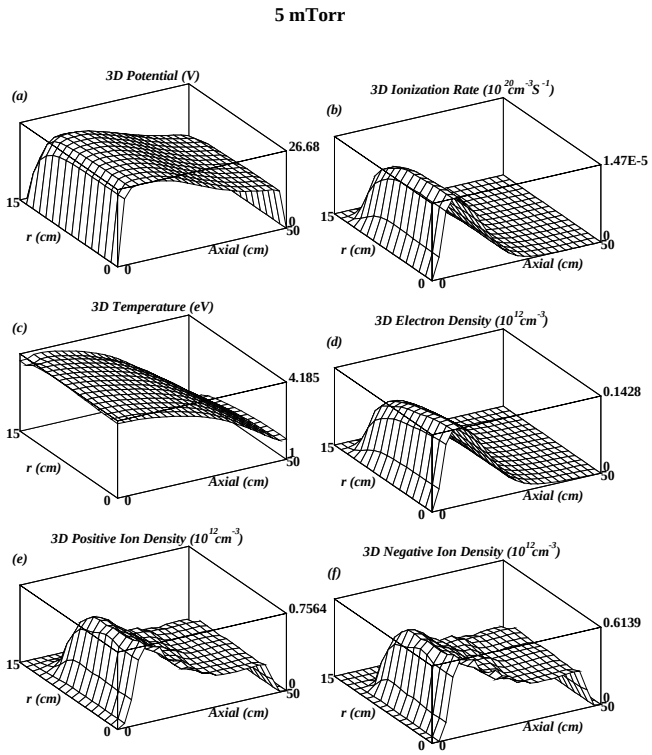

Fig. 3. Profiles of potential, ionization rate, electron temperature, electron density, positive ion density, and negative ion density for 5 mTorr oxygen plasma.

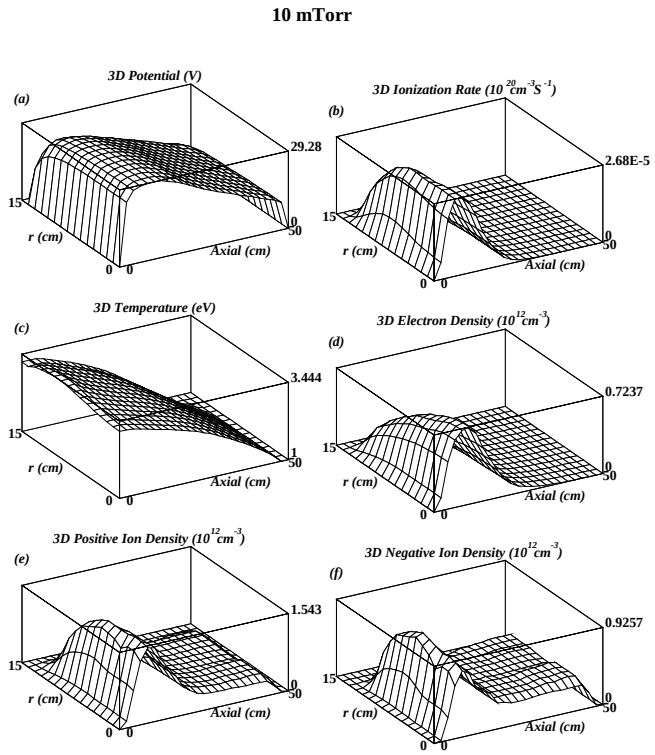

Fig. 4. Profiles of potential, ionization rate, electron temperature, electron density, positive ion density, and negative ion density for 10 mTorr oxygen plasma.

R_{iz}, electron temperature T_e, electron density n_e, positive ion density n_p, and negative ion density n_n, all of which reached the steady state, are plotted for the case of nonuniform power deposition for 5 mTorr pressure oxygen plasma. The ionization rate is almost uniform in the radial direction in the bulk region. At low pressure ($\leq$ 5 mTorr), other types of power deposition profile[1)] such as an exponentially decreasing profile ($P = P_0 e^{-z/\delta}$) are found to have little effect on the plasma density profile.

When the gas pressure is increased to 10 mTorr, as shown in Fig. 4, the plasma potential increases and charged particle densities (n_e, n_n, and n_p) are also increased by a small amount. The ionization rate profile is the result of the combined effect of the electron density and the electron temperature. The ionization rate is higher in the radially centered region than in the radial sheath region. The spatial profiles for ionization rate and electron density are very similar. The effect of localized heating near the roof is clearly evident by the axial variation of the electron temperature which peaked below the dielectric window roof. The resulting electron temperature profile is high on the source side so that the electron temperature gradients are steep. The resulting temperature dependent ionization rate R_{iz} is larger in the source region than in regions farther from the coil. The density profiles are significantly altered by the asymmetry of the source region. The electron density begins to decrease near the axial midpoint, whereas the ion densities (n_n and n_p) have a smooth transition approaching the axial bottom. Quasineutrality ($n_e + n_n \simeq n_p$) exists in the entire plasma region. The positive ion density for the 10 mTorr discharge has a maximum value of about 1.5×10^{12} cm^{-3} which exceeds the electron density. Also, on a reactor-volume-averaged basis, the electronegativity (n_n/n_e) is higher than unity. The negative ion densities are two to three times larger than the electron density, while the peak plasma potential is about 29 V. This is due to the low-power operation. As the absorbed power increases, the electron density becomes larger than the negative ion density. In this model, the O^- ions are essentially at room temperature. Since they are not energetic enough to scale the plasma potential to higher values, the O^- ions pool at the peak of the plasma potential. The off-axis maximum along the radial direction in the O^- density is a good indication of the location of maximum in the plasma potential.

Applied power to the antenna at 13.56 MHz generates an oscillating plasma and produces an azimuthal electric field, as shown schematically in Fig. 1. In an ideal reactor, the azimuthal electric field E_θ is zero on the axis and zero on the periphery, thereby peaking in an annular region at roughly two-thirds the radius. Hence, in Fig. 5, the coil shape could penetrate through the entire plasma so that the coil image could be transferred into the plasma. The spatial variation in the axial and radial directions is sufficient to sharply maximize R_{iz} at large r, and to cause the ionization rate to peak off axis. The O_2^+ density and plasma potential have an off-axis maxima coinciding with the toroidal power deposition. Off-axis maxima in the ion density results in a net flux of ions towards the axis. This can only be sustained if there is a "sink" on the axis. In molecular gases, attachment and dissociative recombination provide a volumetric sink which can sustain an off-axis maxima. Radial fluxes from an off-axis maximum can be redirected towards the upper and lower boundaries and thereby sustain the off-axis maxima.[26)] The ionization rate is almost zero outside the power deposited region and has peaks near the radial plasma sheath boundary. The off-axis maxima in

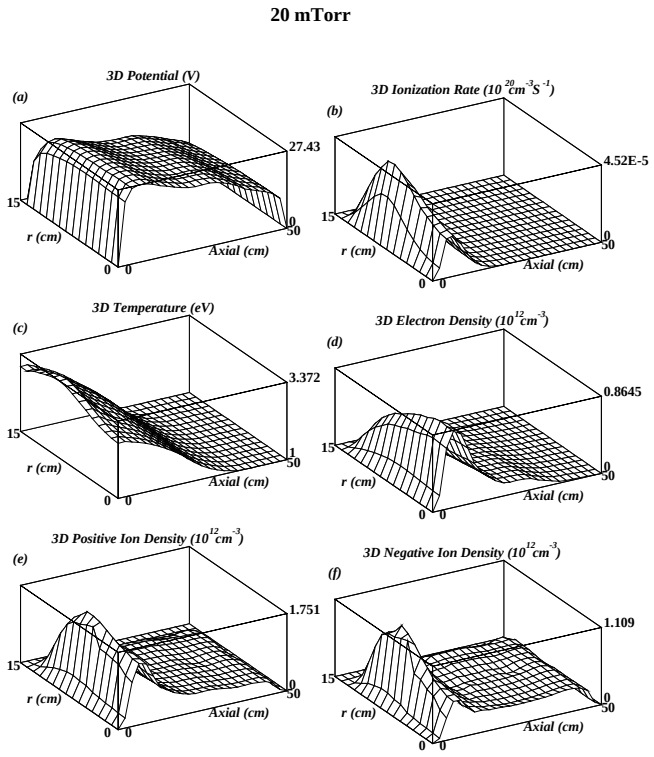

Fig. 5. Profiles of potential, ionization rate, electron temperature, electron density, positive ion density, and negative ion density for 20 mTorr oxygen plasma.

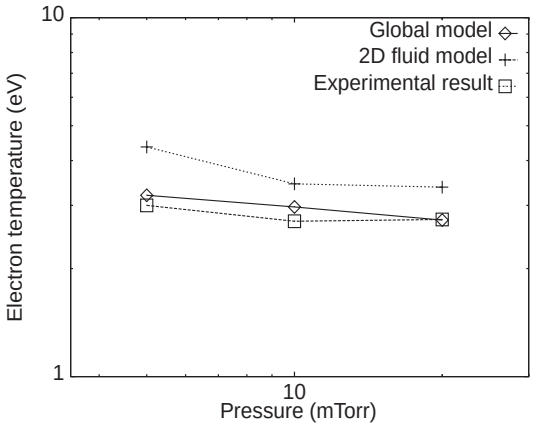

Fig. 6. Electron temperature as a function of pressure.

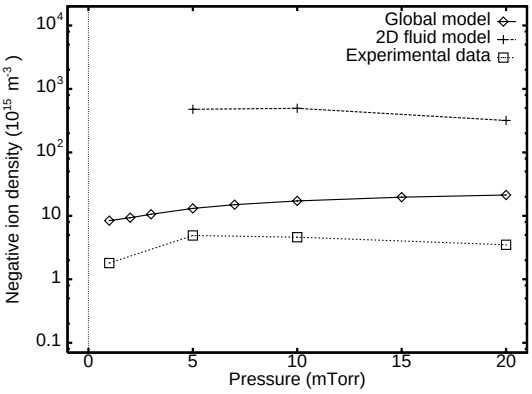

Fig. 7. Negative ion densitiy as a function of pressure at 200 W, and comparison of model results with experimental data.

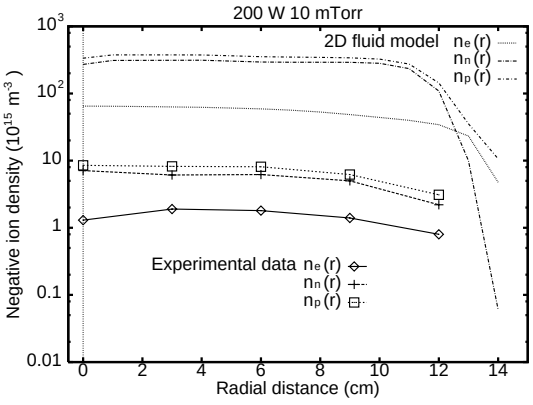

Fig. 8. Profiles of electron, negative ion, and positive ion density along the radial direction at the center of the axial direction ($z = 25$ cm) are shown, and simulation results are compared to experimental results.

the negative ion density, typical for 2D discharges, are clearly observed. The negative ions are generated by the electron attachment, which is high where the electron temperature has a large value. Hence, the negative ion density peaks off-axis below the quartz window where the electron temperature and electron density have large values.

In this study, the effect of gas pressure on the electron temperature is investigated. In Fig. 6, we note that the results of the simulation agree reasonably well with the results of the global model and experimental results.[20] The difference may be due to the neutral gas uniformity assumption. The global model can provide a quick estimation whereas the fluid model can provide spatial profiles of the parameters.

The pressure dependence of the negative ion density is shown in Fig. 7. In this simple reaction model in which O neutral reactions are ignored, the O^- balance is governed by dissociative attachment to O_2 and ion-ion recombination, which causes its density to increased at low pressure.[15] In Fig. 7, the negative ion density increases as pressure is increased. The 2D fluid simulation, global modeling, and experimental measurements produce similar scaling. However, it is expected that as pressure is increased further the negative ion density will saturate and decreases because the recombination loss dominates over the diffusion loss in medium- or high-pressure regions. The model predicts that the magnitude of the plasma density is primarily determined by the electron power balance, eq. (2.7). This power balance equation neglects other energy losses such as attachment, detachment, pair production, dissociative ionization, and dissociation. The average electron energy loss per collision is thus underestimated. Therefore, the simulation results of the magnitude of the plasma density and the electron temperature are overestimated compared to the experimental results.

The density profiles of charged particles along the radial direction at $z = L/2$ are shown in Fig. 8. Here, the results of 2D fluid simulation are compared with the experimental results. The simulation results have higher values of magnitude by more than the order of one. The reason may be that the electron energy loss is underestimated as mentioned before, and that the calculated absorbed power shown in Fig. 2 is overestimated. We obtain the absorbed power, assuming that the discharge is fully inductive [note that eq. (2.5) is used]. In reality, the discharge is partly inductive and partly capacitive.

Even in the case of the one-turn antenna, capacitive coupling can occur.[27] Therefore, the absorbed power to the plasma is less than that of eq. (2.5), thus, the charged particle densities have lower values than the estimated values. In addition, there may be some power losses due to reflection from the load and power dissipation in the matching network and antenna.

5. Conclusions

A 2D fluid model for ICP oxygen discharge has been presented along with a detailed electronegative discharge physics model. The simulation predicts both the axial and radial variations of potential, ionization rate, electron temperature, and charged particles (electron, positive ion, and negative ion) densities. The effect of gas pressure on the 2D distributions of the plasma properties such as potential, ionization rate, electron temperature, and charged particle densities (n_e, n_n, and n_p) are investigated. The volume-averaged charged particle densities are calculated as a function of gas pressure. The inductive power is found to be deposited toroidally within a skin depth below the dielectric roof. As a consequence of the toroidal inductive power deposition, the peak plasma densities in molecular gas are often off-axis. For a relatively high pressure (20 mTorr), the ionization rate peaks in the radial sheath region, where the power deposition is largest. For a relatively low pressure (5 mTorr), the ionization rate is uniform in the radial direction at the bulk region. Therefore, the uniformity of the negative ions in a planar ICP can be improved with a low-pressure operation. We compared the simulation results with the experimental measurements. Generally good agreement between the model and experimental measurements was obtained. The model can estimate the radial variations of the species fluxes to the substrate which are important in predicting the thin-film deposition and its properties. The model will be extended to include more sophisticated discharge chemistry to describe the discharge precisely.

Acknowledgements

This work was supported by Korea Research Foundation Grant No. BSRI-98-2439, Grant No. 1998-001-D00264, and Hanbit User Programs of Korea Basic Science Institute.

1) R. A. Stewart, P. Vietello and D. B. Graves: J. Vac. Sci. Technol. B **12** (1994) 478.
2) G. Dipeso, V. Vahedi, D. W. Hewett and T. D. Rognlien: J. Vac. Sci. Technol. A **12** (1994) 1387.
3) R. A. Stewart, P. Vietello, D. B. Graves, E. F. Jaeger and L. A. Berry: Plasma Source Sci. Technol. **4** (1995) 36.
4) P. L. G. Ventzek, M. Grapperhaus and M. J. Kushner: J. Vac. Sci. Technol. B **12** (1994) 3118.
5) M. Tuszewski: Phys. Plasma **5** (1998) 1198.
6) J. D. Bukowski, D. B. Graves and P. Vitello: J. Appl. Phys. **80** (1996) 2614.
7) J. P. Boeuf: Phys. Rev. A. **36** (1987) 2782.
8) J. P. Boeuf: J. Appl. Phys. **63** (1988) 1342.
9) J. P. Boeuf and L. C. Pitchford: IEEE Trans. Plasma Sci. **19** (1991) 286.
10) H. J. Yoon and T. H. Chung: J. Kor. Phys. Soc. **34** (1999) 29.
11) D. B. Graves and K. F. Jensen: IEEE Trans. Plasma Sci. **14** (1986) 78.
12) D. B. Graves: J. Appl. Phys. **62** (1987) 88.
13) S. K. Park and D. J. Economou: J. Appl. Phys. **68** (1990) 3904.
14) S. K. Park and D. J. Economou: J. Appl. Phys. **68** (1990) 4888.
15) T. H. Chung, L. Meng, H. J. Yoon and J. K. Lee: Jpn. J. Appl. Phys. **36** (1997) 2874.
16) J. D. P. Passchier and W. J. Goedheer: J. Appl. Phys. **74** (1993) 3744.
17) V. Vahedi, P. Mirrashidi, D. K. Wong and J. Verboncoeur: Xgrafix (ver. 2.01), © Copyright 1991–95 The Regents of the University of California.
18) P. N. Barnes: Plasma Sources Sci. Technol. **6** (1997) 435.
19) W. R. Symthe: *Static and Dynamic Electricity* (Hemisphere Publishing, 1989) 3rd ed., p. 270.
20) T. H. Chung, H. J. Yoon and D. C. Seo: J. Appl. Phys. **86** (1999) 3536.
21) E. Meeks and J. W. Shon: IEEE Trans. Plasma Sci. **23** (1995) 539.
22) D. L. Sharfetter and H. K. Gummel: IEEE Trans. Electron Devices **16** (1969) 64.
23) J. K. Lee, L. Meng, Y. K. Shin, H. J. Lee and T. H. Chung: Jpn. J. Appl. Phys. **36** (1997) 5714.
24) H. Amemiya: J. Phys. Soc. Jpn. **57** (1988) 887.
25) H. Amemiya: Jpn. J. Appl. Phys. **27** (1988) 2423.
26) P. L. G. Ventzek, R. J. Hoekstra and M. J. Kushner: J. Vac. Sci. Technol. B **12** (1994) 461.
27) N. S. Yoon, B. C. Kim, J. G. Yang and S. M. Hwang: IEEE Trans. Plasma Sci. **26** (1998) 190.